

## Article

# A Novel BC<sub>2</sub>N Monolayer as Anode Material for Li-Ion Battery

Xiaowei Chen <sup>1,2,\*</sup>, Jiahe Lin <sup>1,2,†</sup>, Qiubao Lin <sup>1,2</sup>, Renquan Li <sup>1</sup> and Hongsheng He <sup>1</sup>

<sup>1</sup> School of Science, Jimei University, Xiamen 361021, China

<sup>2</sup> Semiconductor Industry and Technology Research Institute, Jimei University, Xiamen 361021, China

\* Correspondence: chenxiaowei@jmu.edu.cn

† These authors contributed equally to this work.

**Abstract:** The stability, mechanical and electronic properties of a BC<sub>2</sub>N monolayer and its potential use as an anode material for Li-ion batteries were explored using the density functional theory calculation. The proposed BC<sub>2</sub>N monolayer shows good thermal and dynamical stabilities, as indicated by the ab initio molecular dynamics simulations and phonon dispersion calculations. The BC<sub>2</sub>N monolayer exhibits highly anisotropic mechanical properties. The electronic structure calculation based on the hybrid functional suggests that the BC<sub>2</sub>N monolayer is an indirect bandgap (~1.8 eV) semiconductor. The BC<sub>2</sub>N monolayer shows linear dichroism and is able to harvest visible and ultraviolet light. To investigate the application of the BC<sub>2</sub>N monolayer as a potential anode material for Li-ion batteries, the Li adsorption and diffusion on the monolayer were studied. The BC<sub>2</sub>N monolayer exhibits a high theoretical capacity of 1098 mAh/g for Li-ion batteries. The calculated diffusion barrier of Li ion is 0.45 eV, suggesting a rapid Li-ion charge and discharge rate. The unique mechanical and optical properties of the BC<sub>2</sub>N monolayer also make it an attractive material for use in advanced nanomechanical and optoelectronic devices.

**Keywords:** 2D materials; li-ion batteries; first-principle calculation



**Citation:** Chen, X.; Lin, J.; Lin, Q.; Li, R.; He, H. A Novel BC<sub>2</sub>N Monolayer as Anode Material for Li-Ion Battery. *Batteries* **2023**, *9*, 315. <https://doi.org/10.3390/batteries9060315>

Academic Editors: Chu Liang, Shaohua Lu and Changshin Jo

Received: 29 March 2023

Revised: 29 May 2023

Accepted: 5 June 2023

Published: 6 June 2023



**Copyright:** © 2023 by the authors. Licensee MDPI, Basel, Switzerland. This article is an open access article distributed under the terms and conditions of the Creative Commons Attribution (CC BY) license (<https://creativecommons.org/licenses/by/4.0/>).

## 1. Introduction

Two-dimensional (2D) layered materials with distinctive chemical and physical properties have garnered great interest in the scientific community over the past few decades. Graphene, a prominent member of the 2D materials family, possesses remarkable electronic and mechanical properties, making it a promising material in various applications [1,2]. For instance, graphene and its derivatives have been proven to be promising electrode materials for lithium-ion batteries (LIBs) [3,4]. The unique structure and large surface area of graphene and its derivatives provide a greater exposed surface and various active adsorption sites for Li ions, while reducing the diffusion distance of metal ions and increasing the interfacial interaction between the electrolyte and anode material [4].

It is widely recognized that carbon is capable of forming an extensive range of allotropes. Through recent advancements in experimental and theoretical techniques, several novel two-dimensional carbon allotropes, such as the planar C<sub>4</sub> sheet, penta-graphene, phagraphene and graphdiyne, have been discovered [5]. The electron configuration of B and N resemble that of C. The difference lies in the fact that they have one electron less or one electron more than element C in their outermost shell. Additionally, their atomic radii are similar to that of element C, with element B having a slightly larger atomic radius and element N having a slightly smaller one. The combination of B, C and N atoms offers the potential for the formation of diverse compositions and allotropes of ternary boron-carbon-nitride (B-C-N) materials [6]. In fact, several B-C-N compounds with different compositions and properties, such as carbon-doped h-BN nanosheets, graphene-like B-C-N monolayers and carbon-rich B<sub>x</sub>C<sub>y</sub>N<sub>z</sub>, have been successfully prepared experimentally [7–18]. In addition, extensive theoretical studies have been conducted to investigate the stability and properties of novel 2D ternary B-C-N compounds [18–35]. However, the majority of

them obtained experimentally were graphene/h-BN composites or graphene with modified edges, and the theoretically predicted 2D B-C-N allotropes have been found to be graphene-like nanosheets with a honeycomb lattice. Only a few 2D B-C-N allotropes, such as the T graphene-like  $(BN)_nC_{8-2n}$  ( $n = 0-4$ ) monolayer and Penta BCN monolayer, which exhibit distinct structural arrangements from the honeycomb lattice, have been theoretically predicted [30,36]. The presence of diverse configurations of C-N, C-B and C-C bonds in 2D B-C-N nanosheets suggests the potential discovery of additional allotropes with diverse structural arrangements and extraordinary mechanical and electronic characteristics, which may exhibit a range of intriguing characteristics, including the efficient absorption of visible light, high stability and exceptional energy storage capabilities.

Additionally, the current anodes, predominantly graphite, have been widely used in LIBs due to their stability and relatively high capacity. However, they have inherent limitations that impede their suitability for future high-energy and high-power LIBs. These limitations include a limited theoretical capacity of 372 mAh/g and low rate capability [37,38]. Carbon nitrides, including a variety of nitrogen-rich graphite analogs, have been recognized for their high nitrogen content and the presence of porous defect sites, which make them suitable for lithium storage [37,39]. However, the practical application of carbon nitrides as anode materials is hindered by their poor electrical conductivity, chemical inertness, and inefficient intercalation/deintercalation processes [40]. To address these challenges, we propose the utilization of a 2D layered material, specifically the B-C-N monolayer, as an innovative anode material for LIBs. The incorporation of N and B atoms in the B-C-N monolayer may result in a high affinity for lithium atoms, enabling a significantly increased theoretical capacity for Li storage. Moreover, the B-C-N monolayer possesses a large surface area, which facilitates efficient Li adsorption and desorption processes. This feature may allow for enhanced lithium storage capacity and improved rate capability, addressing the limited theoretical capacity and low rate capability limitation of conventional graphite anodes.

Herein, we predicted a novel 2D  $BC_2N$  monolayer with interesting mechanical, electronic and energy storage properties. The ab initio molecular dynamics simulations and phonon spectrum calculation indicate the excellent thermal and dynamical stabilities of the proposed  $BC_2N$  monolayer. The  $BC_2N$  monolayer can withstand a maximum stress of  $\sim 21$  N/m, corresponding to a tensile strain of 17%, demonstrating its mechanical flexibility under tensile strain. The  $BC_2N$  monolayer is an indirect bandgap semiconductor and shows strong visual and ultraviolet light absorbance. In addition, the  $BC_2N$  monolayer exhibits a high theoretical capacity of 1098 mAh/g for Li-ion batteries. Furthermore, the low Li diffusion barrier points to a rapid charge and discharge rate for Li-ion batteries. Taking into account all of these properties, it can be inferred that the  $BC_2N$  monolayer has the potential to be used as an Li-ion battery's anode material. The distinctive optical and mechanical properties of  $BC_2N$  render it highly attractive for applications in advanced optoelectronic and nanomechanical devices.

## 2. Stability of $BC_2N$ Monolayer

The proposed  $BC_2N$  monolayer's atomic structure is depicted in Figure 1a,b. The length of the sides of the  $BC_2N$  in the plane of the monolayer are equal, with  $a = b = 4.93$  Å. The angles between the sides in the plane of the monolayer are right angles, with  $\alpha = \beta = 90^\circ$ . Additionally, the angle between the sides in the plane of the monolayer and the out-of-plane direction is  $86.56^\circ$ , denoted by  $\gamma$ . All the N, C and B atoms in the  $BC_2N$  monolayer are three-coordinated. Two distinct types of C atoms, namely C1 and C2, were observed. Each C1 atom forms chemical bonds with two C2 atoms and one N atom, whereas each C2 atom forms bonds with two C1 atoms and one B atom. Additionally, each N atom coordinates with two B atoms and one C1 atom. The bond lengths in  $BC_2N$  monolayer are 1.46 Å for C1-C2, 1.32 Å for C1-N, 1.48 Å for C2-B and 1.50 Å for N-B. The atomic structure of the  $BC_2N$  monolayer proposed in this study is distinct from previously reported experimental and theoretically predicted B-C-N monolayers, which typically exhibit a honeycomb lattice

structure. In order to assess the dynamic stability of the  $\text{BC}_2\text{N}$  monolayers, phonon dispersion calculations were conducted, and the results are presented in Figure 1c. The absence of any imaginary phonon frequencies across the Brillouin zone suggests the good dynamic stability of the  $\text{BC}_2\text{N}$  monolayer. Additionally, we also conducted AIMD simulations at 600 K to investigate the thermal stability of the  $\text{BC}_2\text{N}$  monolayer. A  $3 \times 3 \times 1$  supercell of the  $\text{BC}_2\text{N}$  monolayer was used in the simulations to represent a large enough sample of the 2D material. The results of the simulations, including the structures of the  $\text{BC}_2\text{N}$  monolayer and the overall energy variation, are displayed in Figure 1d. The N, B and C atoms within the  $\text{BC}_2\text{N}$  monolayer were observed to oscillate around their equilibrium positions due to thermal energy; however, the C-N, C-B, B-N and C-C bonds within the  $\text{BC}_2\text{N}$  monolayer remained intact after 10 ps of simulation time. Furthermore, the pair correlation function ( $g(r)$ ) was also calculated and is shown in Figure S1. The peaks in the  $g(r)$  function remain distinct at 300 K, 450 K and 600 K, which suggests the absence of any phase transitions throughout the 10 ps simulation period. Thus, it can be concluded that the  $\text{BC}_2\text{N}$  monolayer is thermally and dynamically stable.

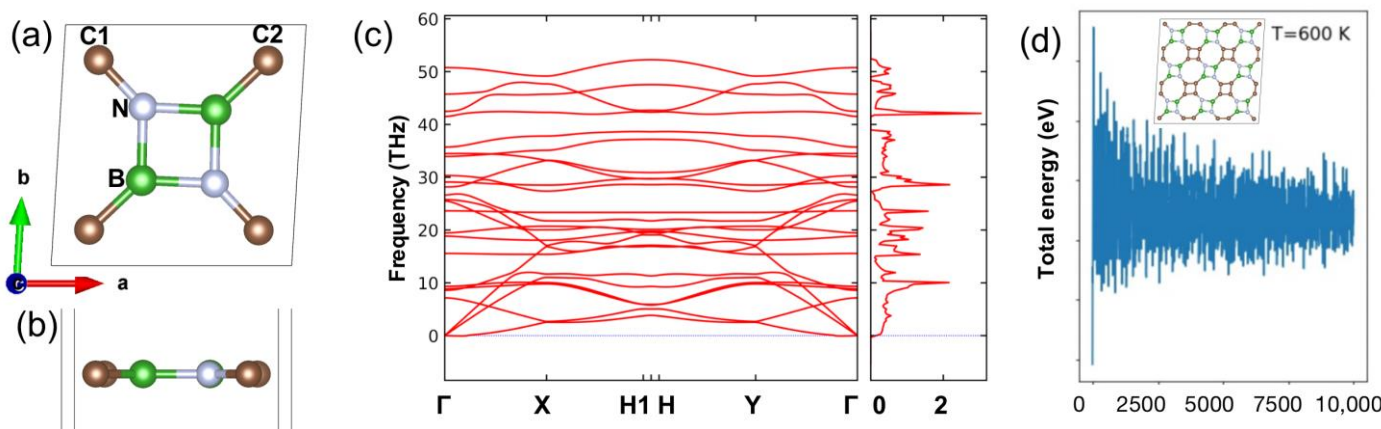


**Figure 1.** The top view (a) and side view of the atomic arrangement in the  $\text{BC}_2\text{N}$  monolayer (b); the phonon spectrum and its associated density of state of  $\text{BC}_2\text{N}$  monolayer (c); fluctuation in total energy during AIMD simulation at 600 K (d).

In order to assess the bond strength in the  $\text{BC}_2\text{N}$  monolayer, crystal orbital Hamilton population (COHP) calculations were performed. The ICOHP value is a quantity determined by performing an integration of the COHP up to the Fermi energy (Table S1). The ICOHP value for the interaction between C1 and C2 atoms in the  $\text{BC}_2\text{N}$  monolayer is 8.78 eV. This value is significantly smaller than the ICOHP value for the C-C interaction in graphene, indicating that the bonding strength between C atoms in the  $\text{BC}_2\text{N}$  monolayer is weaker than in graphene. The reason for the relatively weaker bonding strength between C atoms in the  $\text{BC}_2\text{N}$  monolayer arises from its unique structural arrangement. Specifically, the four C atoms in the monolayer are arranged in a square, which is distinct from the hexagonal structure of graphene. The calculated -ICOHP value for the B-C bond is 8.25 eV, and for the N-B bond, it is 7.54 eV. In contrast, the -ICOHP value for C-N bond is 12.09 eV, which is substantially greater than that for the C-B, C-C and N-B bonds. The bond strengths in the  $\text{BC}_2\text{N}$  monolayer follow the trend: C-N > C-C > B-C > N-B. Based on Bader charge analysis, the charges on the C1, C2, B and N atoms are 0.51, -0.48, 1.57 and  $-1.6\text{ e}^-$ , respectively. This indicates that C1 and B atoms transfer electrons to nearby N atoms, while C2 atoms accept electrons from nearby B atoms. This can be understood from the electronegativity of N, B and C. The B atoms, which have higher electronegativity values than C and N, are expected to transfer electrons to nearby atoms. Additionally, the N atoms, which have lower electronegativity values than C and N, are expected to accept electrons from nearby atoms. The C1 atom coordinates with N atoms to show a positive charge, while the C2 atom coordinates with B atoms to show a negative charge.

### 3. Mechanical Properties

The elastic constants were calculated to further understand the mechanical stability of the BC<sub>2</sub>N monolayer. The elastic modulus  $C_{2D}$  can be estimated by [41]

$$C_{2D} = \frac{(E - E_0)}{S_0} \times \left( \frac{l_0}{\Delta l} \right)^2$$

where  $E_0$ ,  $S_0$  and  $l_0$  represent the total energy, lattice volume and lattice constant of the unstrained BC<sub>2</sub>N, respectively;  $\Delta l$  denotes the deformation and  $E$  is the total energy of the strain BC<sub>2</sub>N.

Poisson's ratio ( $\nu$ ) and Young's modulus ( $Y$ ) are key mechanical properties that characterize the behavior of materials. The Poisson's ratio enables us to evaluate how the BC<sub>2</sub>N monolayer responds to transverse strain when subjected to external loads. Young's modulus provides insights into the material's stiffness or flexibility, allowing us to assess the rigidity of the BC<sub>2</sub>N monolayer. The Young's modulus was calculated as follows:

$$Y_x = (C_{11}C_{22} - C_{12}^2)/C_{22}$$

$$Y_y = (C_{11}C_{22} - C_{12}^2)/C_{11}$$

Additionally, the Poisson's ratio can be obtained using the following equations:

$$\nu_x = C_{21}/C_{22}$$

$$\nu_y = C_{12}/C_{11}$$

The results in Table 1 indicate the mechanical stability of BC<sub>2</sub>N. The  $C_{11}$ ,  $C_{12}$ ,  $C_{22}$ ,  $C_{26}$  and  $C_{66}$  are 198, 119, 200, −14 and 113 J/m<sup>2</sup>, respectively. The mechanical stability criteria of  $C_{11} \times C_{22} > C_{12} \times C_{21}$ ,  $C_{11} > 0$  and  $C_{66} > 0$  [42] are all satisfied. Table 1 shows that the Young's modulus of BC<sub>2</sub>N is nearly identical in both the x and y directions, with a value of ~127 N/m. To investigate the directionally dependent mechanical properties of the BC<sub>2</sub>N monolayer, the dependence of Young's modulus on the angle was calculated. BC<sub>2</sub>N has strong anisotropy in its mechanical properties, as demonstrated by the calculated angular dependency of its Young's modulus (Figure 2a) and Poisson's ratio (Figure 2b). As  $\alpha$  increases from 0° to 45°, the Young's modulus increases from ~127 to 245 N/m but decreases to 128 N/m as  $\alpha$  increases from 45° to 90°, before increasing to its maximum value of 282 N/m when  $\alpha$  increases from 90° to 135°. In contrast to the hexagonal BN sheet (270 N/m), the BC<sub>2</sub>N monolayer has a higher maximum Young's modulus [43].

**Table 1.** Elastic constants, Poisson's ratio ( $\nu$ ) and Young modulus ( $Y$ ) of BC<sub>2</sub>N monolayer.

	$C_{11}$ (J/m <sup>2</sup> )	$C_{12}$ (J/m <sup>2</sup> )	$C_{22}$ (J/m <sup>2</sup> )	$C_{26}$ (J/m <sup>2</sup> )	$C_{66}$ (J/m <sup>2</sup> )	$Y_x$ (N/m)	$Y_y$ (N/m)	$\nu_x$	$\nu_y$
BC <sub>2</sub> N	198	119	200	−14	113	127	127	0.60	0.60

The Young's modulus of BC<sub>2</sub>N can be explained through analyzing the structure and bonding strength of its constituent C-C, C-B, N-C and N-B bonds. In Figure 1a, we observe that the C-C and N-B bonds are aligned parallel to the  $x$ -axis, while the N-C and C-B bonds are oriented at angles of 45° and 135°, respectively, with the  $x$ -axis. Our calculations reveal that the bonding strengths of these bonds follow the following trend: N-C > C-C > C-B > N-B. The relatively low Young's modulus observed at  $\alpha = 0^\circ$  and  $180^\circ$  arise from the relatively weak N-B bonds, which are oriented along the  $x$ -axis. Conversely, the highest Young's modulus observed at  $\alpha = 135^\circ$  is due to the strong N-C bonding strength. The C-B bonding strength is found to be higher than that of C-C and N-B but lower than that of N-C. This explains why Young's modulus at  $\alpha = 45^\circ$  is higher than that at  $\alpha = 0^\circ$  but lower than that at  $\alpha = 135^\circ$ . In terms of Poisson's ratio, the BC<sub>2</sub>N monolayer exhibits a maximum value of 0.60 at  $\alpha = 0^\circ$  and  $90^\circ$  and a minimum value of 0.16 at  $\alpha = 45^\circ$ .

and  $135^\circ$ , further emphasizing its strong anisotropy. When a small amount of strain is applied to the  $\text{BC}_2\text{N}$  sheet, Figure 2c demonstrates that it exhibits a linear stress–strain relationship. As the strain applied to the  $\text{BC}_2\text{N}$  sheet increases, the stress–strain relationship becomes more nonlinear. The maximum stress is  $\sim 21 \text{ N/m}$ , corresponding to a strain of 17% for  $\text{BC}_2\text{N}$ . The previous report suggests a peak stress of  $25 \text{ N/m}$  for the  $\text{B}_4\text{N}$  monolayer [44], which is comparable to the proposed  $\text{BC}_2\text{N}$  monolayer. The stress levels abruptly fall after reaching the maximum tensile point.

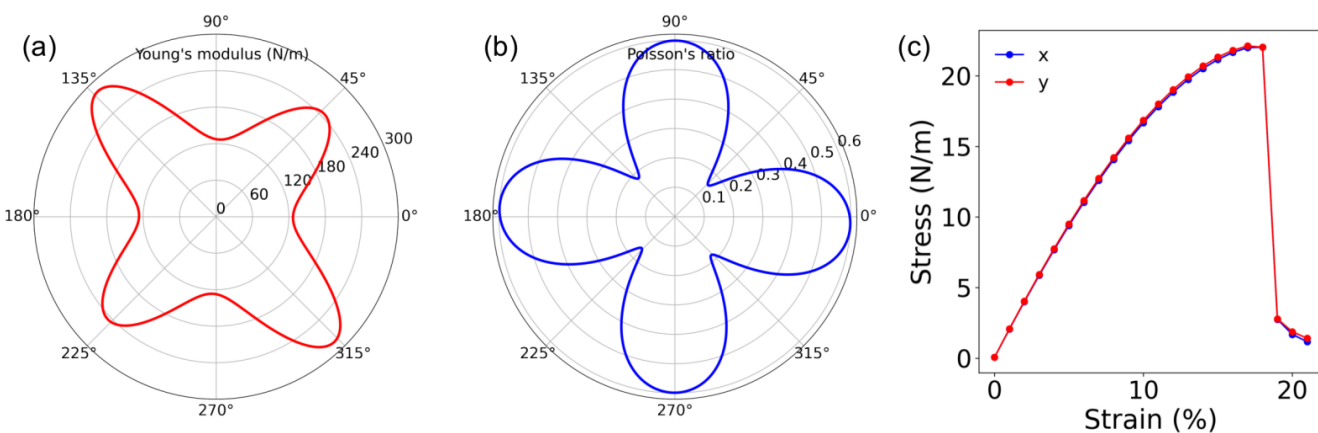


**Figure 2.** The Young's modulus (a), Possion's ration (b) and strain–stress relationship (c) of  $\text{BC}_2\text{N}$  monolayer.

#### 4. Electronic and Optical Properties

We performed band structure and density of states (DOS) calculations by utilizing the HSE06 functional to obtain insights into the electronic properties of the  $\text{BC}_2\text{N}$  monolayer. The calculated 3D band structure (Figure 3a) of the  $\text{BC}_2\text{N}$  monolayer shows that the conduction band minimum (CBM) is located at  $(-0.220, 0.195, 0.000)$  and the valence band maximum (VBM) is located at  $(0.195, 0.171, 0.000)$  in reciprocal space, making  $\text{BC}_2\text{N}$  an indirect bandgap semiconductor with a bandgap of 1.81 eV. The projected DOS (see Figure 3b) reveals that both the conduction band near the CBM and valence band near the Fermi level primarily originate from the  $p$  orbitals of carbon and nitrogen atoms. Hence, the bonding between N and C in the  $\text{BC}_2\text{N}$  monolayer plays a significant role in determining its electronic properties.

Additionally, the optical absorbance of the  $\text{BC}_2\text{N}$  monolayer was further evaluated. To account for the potential impact of the vacuum layer thickness on the optical properties of the 2D material, the normalized absorbance, which is not influenced by the vacuum layer, was calculated. As illustrated in Figure 3c,  $\text{BC}_2\text{N}$  shows a strong optical anisotropy. For the x-polarized light, a broad visible spectrum absorption peak was observed, with its maximum occurring around 580 nm. However, the x-polarized light shows weaker absorption intensity in the same region. In the ultraviolet region, there is a significant absorption peak for y-polarized light, while x-polarized light exhibits comparatively weaker absorption intensity in the same region. The anisotropic absorption behavior of the  $\text{BC}_2\text{N}$  monolayer arises from its distinct atomic structure and electronic properties. The absorption spectra of x-polarized and y-polarized light reflect the different orientations of the  $\text{BC}_2\text{N}$  lattice. The intense absorption in the visible region for x-polarized light is due to the transition of electrons from the valence band to the conduction band, which is mainly contributed to by  $p$  orbitals of C and N atoms. Additionally, the significant transition of electrons from the deep-lying valence band to the conduction band is responsible for the substantial absorption of y-polarized light in the ultraviolet range. The strong optical anisotropy indicates that the  $\text{BC}_2\text{N}$  monolayer can have applications in various optical devices such as polarizers, filters and detectors, where polarization sensitivity is important. The insights gained from our calculations provide a foundation for further experimental

studies aimed at exploring the electronic and optical properties of BC<sub>2</sub>N and its potential applications in various fields.

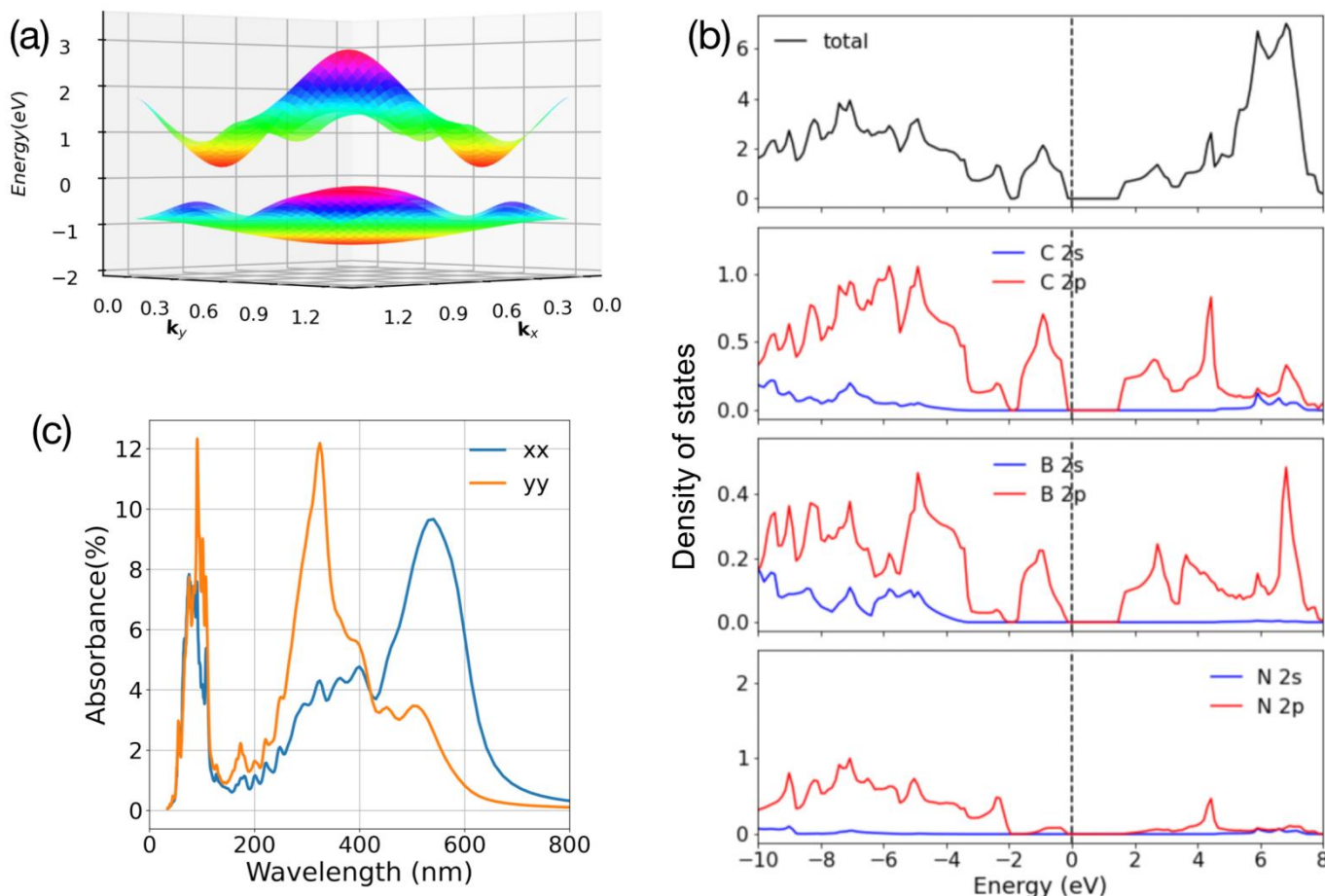


**Figure 3.** The 3D band structure (a), density of state (b) and optical absorbance (c) of the BC<sub>2</sub>N monolayer.

## 5. Li Storage Properties

Our above calculation demonstrates the excellent thermal and dynamical stabilities of BC<sub>2</sub>N. The N and B atoms in BC<sub>2</sub>N may have a high affinity for Li atoms, which allows for a high storage capacity for Li. Moreover, the large surface area of the BC<sub>2</sub>N monolayer may provide ample space for Li adsorption and desorption, making it a promising candidate as an anode material. Hence, we further studied the use of the BC<sub>2</sub>N monolayer as a possible source for the anode in Li-ion batteries.

The results of our analysis indicate that BC<sub>2</sub>N has 16 different Li adsorption sites, including 4 top sites, 3 hollow sites, and 9 bridge sites. We first examined the adsorption of Li atoms on these sites by calculating the absorption energy defined as follows:

$$E_{ads} = E(Li - BC_2N) - E(BC_2N) - E(Li)$$

where  $E(Li)$  denotes the energy of one Li atom from bulk state, and  $E(Li - BC_2N)$  and  $E(BC_2N)$  are the total energy of a  $2 \times 2 \times 1$  supercell of BC<sub>2</sub>N with and without one Li atom adsorption.

We found that the hollow site of the octagon formed by C, N and B and the hollow site of the quadrilateral of C atoms have negative adsorption energies for Li, with respective values of  $-0.62$  eV and  $-0.32$  eV. The hollow site of the octagon shows the lowest Li adsorption energy, indicating that this site is the most stable adsorption site. The Li atoms' adsorption configurations on the hollow site of the octagon are shown in Figure 4a,c. As shown in Figure S2, the total DOS of Li adsorbed on BC<sub>2</sub>N crosses the fermi level, indicating

the metallic feature of the Li adsorption system, which is a desirable property for anode materials in Li-ion batteries. The DOS around the Fermi level is of particular importance as it determines the electronic properties of the BC<sub>2</sub>N. As presented in Figure S2, the *p* orbitals of the C and B atoms are primary contributors to the density of states around the Fermi level. These orbitals likely play an important part in the electronic behavior of the material. Conversely, the N and Li atoms do not seem to significantly affect the density of states around the Fermi level.

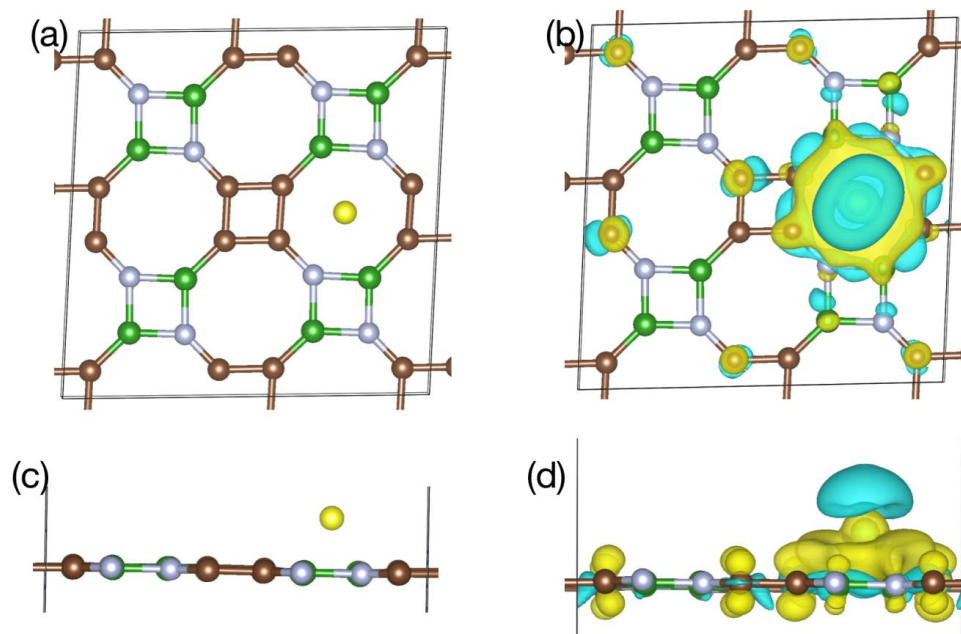


**Figure 4.** The configuration of Li atoms' adsorption with the lowest adsorption energy, as seen from the top (a) and side (c) view; the charge density difference of Li adsorbed on the BC<sub>2</sub>N monolayer, as seen from the top (b) and side (d) view.

The adsorption process of Li atoms on the BC<sub>2</sub>N monolayer can be studied in detail by analyzing the charge density difference using the following formula:

$$\Delta\rho = \rho(Li - BC_2N) - \rho(BC_2N) - \rho(Li)$$

Here,  $\rho(BC_2N)$  and  $\rho(Li - BC_2N)$  refer to the total electron densities of the BC<sub>2</sub>N monolayer and Li adsorbed on the BC<sub>2</sub>N monolayer, respectively, and  $\rho(Li)$  is the total electron density of the Li atom. The observed electron-accumulating region between the Li atoms and the BC<sub>2</sub>N monolayer, as well as the electron-depleting region around the Li atoms (Figure 4b,d), suggest that the adsorbed Li atoms act as electron donors, transferring electrons to the BC<sub>2</sub>N monolayer. The Bader charge before and after Li adsorption is shown in Table S1. The transfer of charge from Li to the BC<sub>2</sub>N monolayer is further supported by the Bader charge analysis, which reveals a total transfer of 0.75 e<sup>-</sup> from Li to BC<sub>2</sub>N. The C2 atom near Li accepts more electrons compared to that in BC<sub>2</sub>N. Intriguingly, away from the Li adsorption site, the charge density difference plots also show a small electron-accumulating region around the C1 atoms. On the other hand, the absence of charge transfer or electron-accumulating regions around the C2 atoms (away from the Li adsorption site) suggests that these atoms are not significantly affected by the adsorption of Li. This may be due to the specific electronic properties of the C2 atoms or their location within the BC<sub>2</sub>N monolayer.

The mobility of Li ions is important in determining the rate of charge/discharge, as well as the overall capacity and lifespan of the Li-ion battery. Hence, we further investigated the diffusion of Li within the BC<sub>2</sub>N monolayer using the CI-NEB method. Our study considered two possible diffusion paths, namely path 1 and path 2, as illustrated in Figure 5.

The analysis aimed to shed light on how Li atoms may move from one adsorption site to another within the BC<sub>2</sub>N structure. As shown in Figure 5, for both path 1 and path 2, Li starts from the octagonal hollow site of BC<sub>2</sub>N, and then passes through the local minimum energy position near the carbon tetragonal hollow site and finally reaches the near octagonal hollow site. In both Li diffusion paths, the energy barriers are 0.45 eV, which suggests that the movement of Li is equally easy in both directions. The Li diffusion barriers in BC<sub>2</sub>N are similar to that of Θ-graphene (0.48 eV) [45] and lower than that of β12/χ3 borophene [46]. This suggests that the BC<sub>2</sub>N monolayer has the potential to be a promising candidate for use in lithium-ion batteries, as it allows for easy and efficient Li diffusion.

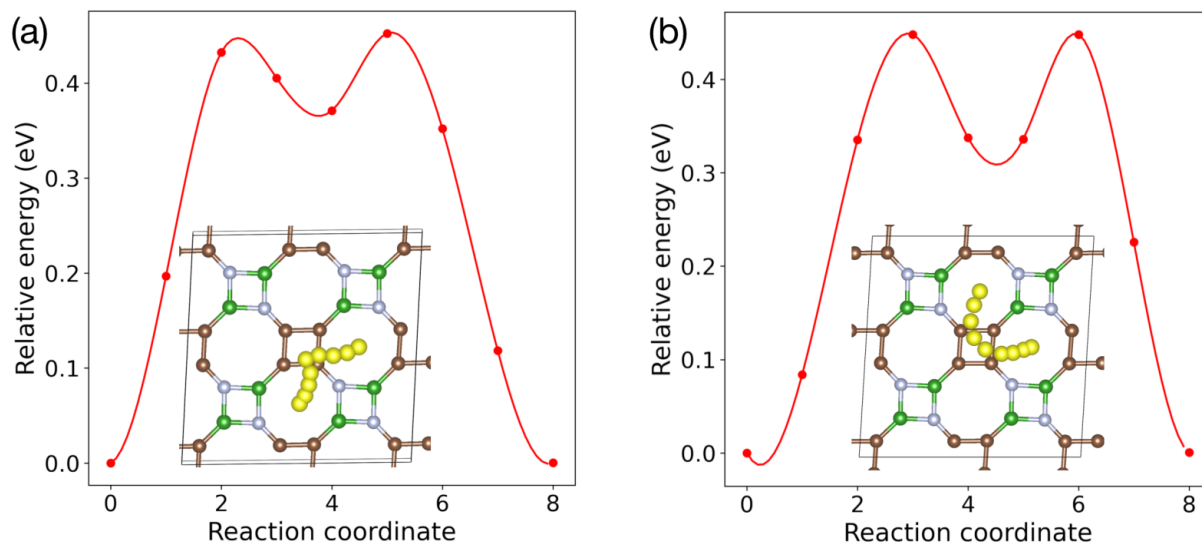


**Figure 5.** The relative energy profile of Li diffusion path1 (a) and path2 (b). The insert represents the diffusion path of Li. The diffusion Li atom is denoted as yellow balls.

It is crucial to investigate the storage capacity and open-circuit voltages (OCVs) to evaluate the applications of BC<sub>2</sub>N as an anode material. The following equation is used to determine the maximum Li-ion storage capacity:

$$C(\text{mAh/g}) = \frac{n \times F}{\text{mass(BC}_2\text{N)}}$$

where  $n$  is the maximum number of Li atoms that can adsorb on a  $2 \times 2 \times 1$  supercell of the BC<sub>2</sub>N monolayer, mass (BC<sub>2</sub>N) is the molecular weight of the  $2 \times 2 \times 1$  supercell of BC<sub>2</sub>N, and  $F$  is the Faraday constant.

The average open-circuit voltages are calculated as

$$V = \frac{E(n\text{Li} - \text{BC}_2\text{N}) - E(\text{BC}_2\text{N}) - nE(\text{Li})}{n}$$

$E(\text{Li})$  corresponds to the energy of a single Li atom in its bulk state. Additionally, the values of  $E(n\text{Li} - \text{BC}_2\text{N})$  and  $E(\text{BC}_2\text{N})$  represent the total energy of the BC<sub>2</sub>N supercell with and without the adsorption of  $n$  number of Li atoms, respectively.

To determine the maximum capacity of the BC<sub>2</sub>N monolayer as an anode material, we gradually increased the adsorption of Li on BC<sub>2</sub>N (see Figure 6b–f). We only considered two Li layers on either side of BC<sub>2</sub>N and used a  $2 \times 2 \times 1$  supercell for this purpose. First, we fully adsorbed the first layer of Li and then added subsequent Li atoms to BC<sub>2</sub>N on both sides by considering the second layer. The open-circuit voltages of a system generally reflect the energy required to initiate electrochemical reactions, with higher voltages indicating greater thermodynamic stability. In the case of Li atoms' adsorption on the BC<sub>2</sub>N monolayer,

Figure 6a shows that as the amount of adsorbed Li atoms grows from 1 to 16, the open-circuit voltages steadily fall from 0.63 V to 0.12 V. This indicates that the system becomes progressively less stable as more Li atoms are added, likely due to the increased Coulombic repulsion between the adsorbed Li atoms. However, the stability of the system takes a dramatic turn beyond the 16th Li atom, as further increasing the adsorbed Li atoms leads to a significant decrease in the open-circuit voltages to near zero. This implies that the system becomes increasingly unstable, with the added Li atoms destabilizing the adsorption site and potentially triggering undesired electrochemical reactions. Previous theoretical studies have identified the nitrogenated holey graphene C<sub>2</sub>N monolayer as an excellent candidate for Li-ion battery anodes [47]. In the case of the C<sub>2</sub>N monolayer, the open-circuit voltages (OCVs) consistently decrease from 1.2 V to 0.1 V as the number of adsorbed Li atoms increases [47], mirroring the trend observed in BC<sub>2</sub>N. At lower Li concentrations, the OCVs of BC<sub>2</sub>N are lower than those of C<sub>2</sub>N, potentially due to variances in elemental composition and atomic arrangement. However, at higher Li concentrations, both BC<sub>2</sub>N and C<sub>2</sub>N exhibit similar OCVs of 0.1 V. From the above calculation, it can be seen that the 2 × 2 × 1 supercell of BC<sub>2</sub>N can adsorb up to 16 Li atoms, corresponding to a maximum capacity of 1098 mAh/g, which is comparable to other 2D carbon anodes, including xgraphene, and is greater than the capacity of graphite (372 mAh/g) [48]. The results of high Li storage capacity and low OCVs suggest that BC<sub>2</sub>N can be a potential anode material for LIBs. Further experimental investigations are necessary to validate these findings and assess the feasibility of utilizing BC<sub>2</sub>N as an anode material in LIBs.

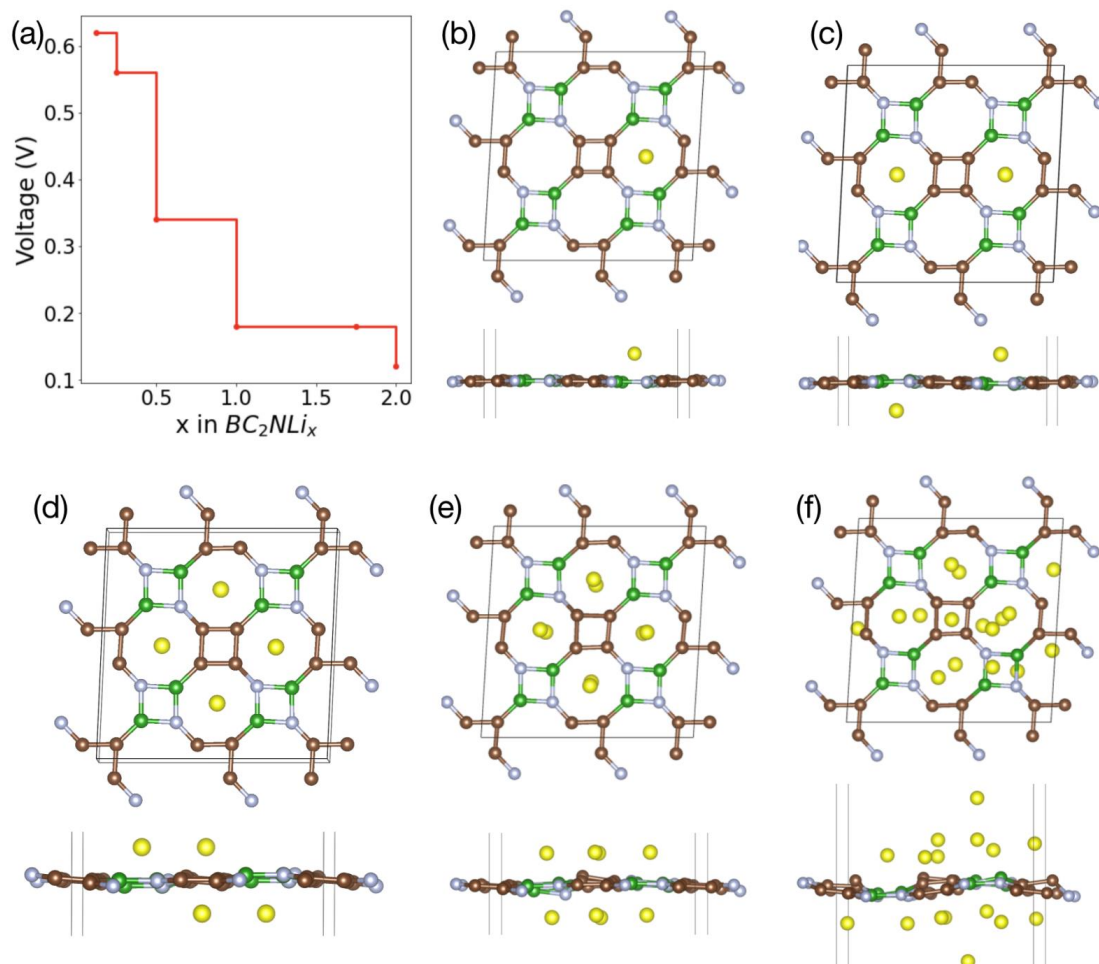


**Figure 6.** The open-circuit voltages (a) and the configuration for one (b), two (c), four (d), eight (e) and sixteen (f) Li atoms on the BC<sub>2</sub>N monolayer.

## 6. Conclusions

We proposed a novel 2D BC<sub>2</sub>N monolayer using DFT calculation. The ab initio molecular dynamics simulations and phonon spectrum indicate the excellent thermal and dynamical stabilities of the proposed BC<sub>2</sub>N monolayer. The BC<sub>2</sub>N monolayer monolayers can withstand a maximum tensile strain of 17%, corresponding to a stress of ~21 N/m, demonstrating its mechanical flexibility under tensile strain. The BC<sub>2</sub>N monolayer is an indirect bandgap (~1.8 eV) semiconductor and shows strong visual and ultraviolet light absorbance. Furthermore, the BC<sub>2</sub>N monolayer displays a remarkable theoretical capacity of 1098 mAh/g for Li-ion batteries, which is three times higher compared to graphite. This significant improvement in capacity highlights the potential of BC<sub>2</sub>N as a highly promising alternative for achieving higher energy storage capabilities in lithium-ion battery systems. Additionally, the diffusion barrier of Li is only 0.45 eV, which suggests a rapid charge and discharge rate for Li-ion batteries. All these desirable properties make the BC<sub>2</sub>N monolayer a potential anode material for Li-ion batteries. In addition, exceptional optical and mechanical properties exhibited by the BC<sub>2</sub>N monolayer render it highly attractive for utilization in cutting-edge optoelectronic and nanomechanical devices.

**Supplementary Materials:** The following supporting information can be downloaded at: <https://www.mdpi.com/article/10.3390/batteries9060315/s1>, Figure S1: Pair correlation function of BC<sub>2</sub>N monolayer; Figure S2: The density of state of Li adsorb on BC<sub>2</sub>N monolayer. Table S1: The -ICOHP value for the C1-C2, C-B, C-N and N-B bonds; Table S2: Bader charge of BC<sub>2</sub>N monolayer without and with Li adsorption. The C, B and N bader charge of Li adsorption BC<sub>2</sub>N monolayer were selected near the Li atom [30,42,49–56].

**Author Contributions:** Conceptualization, X.C. and J.L.; methodology, X.C. and J.L.; software, R.L. and H.H.; validation, X.C. and J.L.; formal analysis, X.C.; investigation, X.C.; resources, X.C. and Q.L.; data curation, R.L. and H.H.; writing—original draft preparation, X.C.; writing—review and editing, X.C.; visualization, R.L. and H.H.; supervision, X.C.; project administration, X.C.; funding acquisition, X.C., J.L. and Q.L. All authors have read and agreed to the published version of the manuscript.

**Funding:** This research was funded by the National Natural Science Foundation of China (52071156, 12204195), Natural Science Foundation of Fujian Province (2020J05147) and Scientific Research Starting Foundation of Jimei University (China) (ZQ2019015).

**Data Availability Statement:** Data is contained within the article or supplementary material.

**Conflicts of Interest:** The authors declare no conflict of interest.

## References

1. Olabi, A.G.; Abdelkareem, M.A.; Wilberforce, T.; Sayed, E.T. Application of graphene in energy storage device—A review. *Renew. Sustain. Energy Rev.* **2021**, *135*, 110026. [[CrossRef](#)]
2. Huang, H.; Shi, H.; Das, P.; Qin, J.; Li, Y.; Wang, X.; Su, F.; Wen, P.; Li, S.; Lu, P. The chemistry and promising applications of graphene and porous graphene materials. *Adv. Funct. Mater.* **2020**, *30*, 1909035. [[CrossRef](#)]
3. Rojaee, R.; Shahbazian-Yassar, R. Two-dimensional materials to address the lithium battery challenges. *ACS Nano* **2020**, *14*, 2628–2658. [[CrossRef](#)] [[PubMed](#)]
4. Dai, C.; Sun, G.; Hu, L.; Xiao, Y.; Zhang, Z.; Qu, L. Recent progress in graphene-based electrodes for flexible batteries. *InfoMat* **2020**, *2*, 509–526. [[CrossRef](#)]
5. Chen, Y.; Xie, Y.; Yan, X.; Cohen, M.L.; Zhang, S. Topological carbon materials: A new perspective. *Phys. Rep.* **2020**, *868*, 1–32. [[CrossRef](#)]
6. Nehate, S.D.; Saikumar, A.K.; Prakash, A.; Sundaram, K.B. A review of boron carbon nitride thin films and progress in nanomaterials. *Mater. Today Adv.* **2020**, *8*, 100106. [[CrossRef](#)]
7. Kida, T.; Shigezumi, K.; Mannan, M.A.; Akiyama, M.; Baba, Y.; Nagano, M. Synthesis of boron carbonitride (BCN) films by plasma-enhanced chemical vapor deposition using trimethylamine borane as a molecular precursor. *Vacuum* **2009**, *83*, 1143–1146. [[CrossRef](#)]
8. Ci, L.; Song, L.; Jin, C.; Jariwala, D.; Wu, D.; Li, Y.; Srivastava, A.; Wang, Z.F.; Storr, K.; Balicas, L.; et al. Atomic layers of hybridized boron nitride and graphene domains. *Nat. Mater.* **2010**, *9*, 430–435. [[CrossRef](#)]
9. Huang, C.; Chen, C.; Zhang, M.; Lin, L.; Ye, X.; Lin, S.; Antonietti, M.; Wang, X. Carbon-doped BN nanosheets for metal-free photoredox catalysis. *Nat. Commun.* **2015**, *6*, 7698. [[CrossRef](#)]

10. Zhang, K.; Feng, Y.; Wang, F.; Yang, Z.; Wang, J. Two dimensional hexagonal boron nitride (2D-hBN): Synthesis, properties and applications. *J. Mater. Chem. C* **2017**, *5*, 11992–12022. [[CrossRef](#)]
11. Chhetri, M.; Maitra, S.; Chakraborty, H.; Waghmare, U.V.; Rao, C. Superior performance of borocarbonitrides,  $B_xC_yN_z$ , as stable, low-cost metal-free electrocatalysts for the hydrogen evolution reaction. *Energy Environ. Sci.* **2016**, *9*, 95–101. [[CrossRef](#)]
12. Fiori, G.; Betti, A.; Bruzzone, S.; Iannaccone, G. Lateral graphene–hBCN heterostructures as a platform for fully two-dimensional transistors. *ACS Nano* **2012**, *6*, 2642–2648. [[CrossRef](#)]
13. Beniwal, S.; Hooper, J.; Miller, D.P.; Costa, P.S.; Chen, G.; Liu, S.Y.; Dowben, P.A.; Sykes, E.C.; Zurek, E.; Enders, A. Graphene-like Boron-Carbon-Nitrogen Monolayers. *ACS Nano* **2017**, *11*, 2486–2493. [[CrossRef](#)]
14. Rao, C.N.R.; Gopalakrishnan, K. Borocarbonitrides,  $B(x)C(y)N(z)$ : Synthesis, Characterization, and Properties with Potential Applications. *ACS Appl. Mater. Interfaces* **2017**, *9*, 19478–19494. [[CrossRef](#)] [[PubMed](#)]
15. Mou, P.; Zhao, J.; Wang, G.; Shi, S.; Wan, G.; Zhou, M.; Deng, Z.; Teng, S.; Wang, G. BCN nanosheets derived from coconut shells with outstanding microwave absorption and thermal conductive properties. *Chem. Eng. J.* **2022**, *437*, 135285. [[CrossRef](#)]
16. Hasan, M.M.; Khedr, G.E.; Zakaria, F.; Allam, N.K. Intermolecular electron transfer in electrochemically exfoliated BCN-Cu nanosheet electrocatalysts for efficient hydrogen evolution. *ACS Appl. Energy Mater.* **2022**, *5*, 9692–9701. [[CrossRef](#)]
17. Kaur, M.; Singh, K.; Vij, A.; Kumar, A. Recent insights into BCN nanomaterials—Synthesis, properties and applications. *New J. Chem.* **2023**, *47*, 2137–2160. [[CrossRef](#)]
18. Seo, T.H.; Lee, W.; Lee, K.S.; Hwang, J.Y.; Son, D.I.; Ahn, S.; Cho, H.; Kim, M.J. Dominant formation of h-BC2N in h-BxCyNz films: CVD synthesis and characterization. *Carbon* **2021**, *182*, 791–798. [[CrossRef](#)]
19. Lam, K.-T.; Lu, Y.; Feng, Y.P.; Liang, G. Stability and electronic structure of two dimensional  $C_x(BN)_y$  compound. *Appl. Phys. Lett.* **2011**, *98*, 022101. [[CrossRef](#)]
20. Bafecky, A.; Naseri, M.; Fadlallah, M.M.; Abdolhosseini Sarsari, I.; Faraji, M.; Bagheri Khatibani, A.; Ghergherehchi, M.; Gogova, D. A novel two-dimensional boron–carbon–nitride (BCN) monolayer: A first-principles insight. *J. Appl. Phys.* **2021**, *130*, 114301. [[CrossRef](#)]
21. Zhang, M.; Gao, G.; Kutana, A.; Wang, Y.; Zou, X.; Tse, J.S.; Yakobson, B.I.; Li, H.; Liu, H.; Ma, Y. Two-dimensional boron-nitrogen-carbon monolayers with tunable direct band gaps. *Nanoscale* **2015**, *7*, 12023–12029. [[CrossRef](#)]
22. Sun, J.; Zhou, X.-F.; Chen, J.; Fan, Y.-X.; Wang, H.-T.; Guo, X.; He, J.; Tian, Y. Infrared and Raman spectra of  $\beta$ -BC2N from first principles calculations. *Phys. Rev. B* **2006**, *74*, 193101. [[CrossRef](#)]
23. Lu, Y.; Zhu, X.; Wang, M. Theoretical investigations of a new two-dimensional semiconducting boron-carbon-nitrogen structure. *RSC Adv.* **2020**, *10*, 3424–3428. [[CrossRef](#)] [[PubMed](#)]
24. Barbosa, R.C.; Guimarães, P.S.; Baierle, R.J. First principles study of native defects in a graphitic BC2N monolayer. *Thin Solid Film.* **2010**, *518*, 4356–4362. [[CrossRef](#)]
25. Xie, J.; Zhang, Z.Y.; Yang, D.Z.; Xue, D.S.; Si, M.S. Theoretical Prediction of Carrier Mobility in Few-Layer BC2N. *J. Phys. Chem. Lett.* **2014**, *5*, 4073–4077. [[CrossRef](#)]
26. Zhang, H.; Li, X.; Meng, X.; Zhou, S.; Yang, G.; Zhou, X. Isoelectronic analogues of graphene: The BCN monolayers with visible-light absorption and high carrier mobility. *J. Phys. Condens. Matter* **2019**, *31*, 125301. [[CrossRef](#)]
27. Alyörük, M.M. Piezoelectricity in monolayer BxCyNz structures: A first principles study. *Comput. Mater. Sci.* **2021**, *195*, 110505. [[CrossRef](#)]
28. Bafecky, A.; Naseri, M.; Faraji, M.; Fadlallah, M.M.; Hoat, D.M.; Jappor, H.R.; Ghergherehchi, M.; Gogova, D.; Afarideh, H. Theoretical prediction of two-dimensional BC2X (X = N, P, As) monolayers: Ab initio investigations. *Sci. Rep.* **2022**, *12*, 22269. [[CrossRef](#)]
29. Yu, J.; He, C.; Huo, J.; Zhao, C.; Yu, L. Electric field controlled CO<sub>2</sub> capture and activation on BC6N monolayers: A first-principles study. *Surf. Interfaces* **2022**, *30*, 101885. [[CrossRef](#)]
30. Chen, L.; Yang, M.; Kong, F.; Du, W.; Guo, J.; Shu, H. Penta-BCN monolayer with high specific capacity and mobility as a compelling anode material for rechargeable batteries. *Phys. Chem. Chem. Phys.* **2021**, *23*, 17693–17702. [[CrossRef](#)]
31. Kilic, M.E.; Lee, K.-R. Emerging exotic properties of two-dimensional ternary tetrahexagonal BCN: Tunable anisotropic transport properties with huge excitonic effects for nanoelectronics and optoelectronics. *Mater. Today Phys.* **2022**, *27*, 100792. [[CrossRef](#)]
32. Kilic, M.E.; Lee, K.-R. Two-Dimensional Ternary Pentagonal BCN: A Promising Photocatalyst Semiconductor for Water Splitting with Strong Excitonic Effects. *Phys. Rev. Appl.* **2022**, *18*, 014066. [[CrossRef](#)]
33. Dabsamut, K.; Thanasarnsurapong, T.; Maluangnont, T.; Jiraroj, T.; Junghawan, S.; Boonchun, A. Strain engineering and thermal conductivity of a penta-BCN monolayer: A computational study. *J. Phys. D Appl. Phys.* **2021**, *54*, 355301. [[CrossRef](#)]
34. Matar, S.F.; Solozhenko, V.L. New superhard tetragonal BCN from crystal chemistry and first principles. *Materialia* **2022**, *26*, 101581. [[CrossRef](#)]
35. Ananchuensook, A.; Dabsamut, K.; Thanasarnsurapong, T.; Maluangnont, T.; Jiraroj, T.; Junghawan, S.; Boonchun, A. Towards a new packing pattern of Li adsorption in two-dimensional pentagonal BCN. *Phys. Chem. Chem. Phys.* **2022**, *24*, 13194–13200. [[CrossRef](#)]
36. Majidi, R. Electronic properties of T graphene-like C-BN sheets: A density functional theory study. *Phys. E Low-Dimens. Syst. Nanostruct.* **2015**, *74*, 371–376. [[CrossRef](#)]
37. Adekoya, D.; Qian, S.; Gu, X.; Wen, W.; Li, D.; Ma, J.; Zhang, S. DFT-guided design and fabrication of carbon-nitride-based materials for energy storage devices: A review. *Nano Micro Lett.* **2021**, *13*, 13. [[CrossRef](#)]

38. Sun, Y.; Yang, T.; Ji, H.; Zhou, J.; Wang, Z.; Qian, T.; Yan, C. Boosting the optimization of lithium metal batteries by molecular dynamics simulations: A perspective. *Adv. Energy Mater.* **2020**, *10*, 2002373. [[CrossRef](#)]
39. He, B.; Wang, Y.; Zhai, Q.; Qiu, P.; Dong, G.; Liu, X.; Chen, Y.; Li, Z. From polymeric carbon nitride to carbon materials: Extended application to electrochemical energy conversion and storage. *Nanoscale* **2020**, *12*, 8636–8646. [[CrossRef](#)]
40. Chen, J.; Mao, Z.; Zhang, L.; Wang, D.; Xu, R.; Bie, L.; Fahlman, B.D. Nitrogen-deficient graphitic carbon nitride with enhanced performance for lithium ion battery anodes. *ACS Nano* **2017**, *11*, 12650–12657. [[CrossRef](#)]
41. Le Page, Y.; Saxe, P. Symmetry-general least-squares extraction of elastic coefficients from ab initio total energy calculations. *Phys. Rev. B* **2001**, *63*, 174103. [[CrossRef](#)]
42. Wang, V.; Xu, N.; Liu, J.-C.; Tang, G.; Geng, W.-T. VASPKIT: A user-friendly interface facilitating high-throughput computing and analysis using VASP code. *Comput. Phys. Commun.* **2021**, *267*, 108033. [[CrossRef](#)]
43. Kudin, K.N.; Scuseria, G.E.; Yakobson, B.I. C 2 F, BN, and C nanoshell elasticity from ab initio computations. *Phys. Rev. B* **2001**, *64*, 235406. [[CrossRef](#)]
44. Wang, B.; Wu, Q.; Zhang, Y.; Ma, L.; Wang, J. Auxetic B(4)N Monolayer: A Promising 2D Material with in-Plane Negative Poisson’s Ratio and Large Anisotropic Mechanics. *ACS Appl. Mater. Interfaces* **2019**, *11*, 33231–33237. [[CrossRef](#)]
45. Wang, S.; Yang, B.; Chen, H.; Ruckenstein, E. Reconfiguring graphene for high-performance metal-ion battery anodes. *Energy Storage Mater.* **2019**, *16*, 619–624. [[CrossRef](#)]
46. Zhang, X.; Hu, J.; Cheng, Y.; Yang, H.Y.; Yao, Y.; Yang, S.A. Borophene as an extremely high capacity electrode material for Li-ion and Na-ion batteries. *Nanoscale* **2016**, *8*, 15340–15347. [[CrossRef](#)]
47. Wu, D.; Yang, B.; Chen, H.; Ruckenstein, E. Nitrogenated holey graphene C2N monolayer anodes for lithium-and sodium-ion batteries with high performance. *Energy Storage Mater.* **2019**, *16*, 574–580. [[CrossRef](#)]
48. Wang, S.; Si, Y.; Yang, B.; Ruckenstein, E.; Chen, H. Two-dimensional carbon-based auxetic materials for broad-spectrum metal-ion battery anodes. *J. Phys. Chem. Lett.* **2019**, *10*, 3269–3275. [[CrossRef](#)]
49. Kresse, G.; Furthmüller, J. Efficient Iterative Schemes for Ab Initio Total-Energy Calculations Using a Plane-Wave Basis Set. *Phys. Rev. B* **1996**, *54*, 11169. [[CrossRef](#)]
50. Blöchl, P.E. Projector Augmented-Wave Method. *Phys. Rev. B* **1994**, *50*, 17953. [[CrossRef](#)]
51. Perdew, J.P.; Burke, K.; Wang, Y. Generalized Gradient Approximation for the Exchange-Correlation Hole of a Many-Electron System. *Phys. Rev. B* **1996**, *54*, 16533–16539. [[CrossRef](#)] [[PubMed](#)]
52. Perdew, J.P.; Burke, K.; Ernzerhof, M. Generalized Gradient Approximation Made Simple. *Phys. Rev. Lett.* **1996**, *77*, 3865–3868. [[CrossRef](#)] [[PubMed](#)]
53. Grimme, S.; Antony, J.; Ehrlich, S.; Krieg, H. A Consistent and Accurate Ab Initio Parametrization of Density Functional Dispersion Correction (Dft-D) for the 94 Elements H-Pu. *J. Chem. Phys.* **2010**, *132*, 154104. [[CrossRef](#)] [[PubMed](#)]
54. Paier, J.; Marsman, M.; Hummer, K.; Kresse, G.; Gerber, I.C.; Ángyán, J.G. Screened Hybrid Density Functionals Applied to Solids. *J. Chem. Phys.* **2006**, *124*, 154709. [[CrossRef](#)] [[PubMed](#)]
55. Parlinski, K.; Li, Z.Q.; Kawazoe, Y. First-Principles Determination of the Soft Mode in Cubic Zro2. *Phys. Rev. Lett.* **1997**, *78*, 4063–4066. [[CrossRef](#)]
56. Henkelman, G.; Uberuaga, B.P.; Jónsson, H. A Climbing Image Nudged Elastic Band Method for Finding Saddle Points and Minimum Energy Paths. *J. Chem. Phys.* **2000**, *113*, 9901–9904. [[CrossRef](#)]

**Disclaimer/Publisher’s Note:** The statements, opinions and data contained in all publications are solely those of the individual author(s) and contributor(s) and not of MDPI and/or the editor(s). MDPI and/or the editor(s) disclaim responsibility for any injury to people or property resulting from any ideas, methods, instructions or products referred to in the content.